

# CHARACTERIZATION OF DUST ACTIVITY FROM MY27 TO MY32 OBSERVED BY PFS-MEX

**P. Wolkenberg**<sup>1,2</sup>, <sup>1</sup>Institute for Space Astrophysics and Planetology (IAPS), National Institute of Astrophysics (INAF), Via del Fosso del Cavaliere 100, 00133 Roma, Italy (*paulina.wolkenberg@iaps.inaf.it*), <sup>2</sup>Centrum Badan Kosmicznych (CBK), Polska Akademia Nauk (PAN), **M. Giuranna**<sup>1</sup>, **S. Aoki**<sup>1,3</sup>, <sup>3</sup>Department of Geophysics, Graduate school of Science, Tohoku University, Aramaki Aza Aoba 6-3, Sendai, Miyagi 980-8578, Japan, **A. Mahieux**<sup>1,3,4</sup>, <sup>4</sup>Institut d'Aéronomie Spatiale de Belgique, avenue Circulaire 3, 1180 Brussels, Belgium

## Introduction:

Dust is one of most variable and meteorologically important component of the Martian atmosphere. It is strongly radiatively active and shows high temporal and spatial variability.

One of the first spaceborne instrument which remotely monitored the atmosphere in the infrared range was the IRIS spectrometer (InfaRed Interferometer Spectrometer, [1]) on-board Mariner 9. The IRIS data was used to describe the post-phase of the global dust storm which occurred in 1971 (MY 9) [2]. Then, the Viking mission [3] observed the Martian atmosphere using the IRTM infrared thermal mapper during two planet-encircling dust storms in 1977 (MY 12) commencing respectively at about  $L_s = 205^\circ$  and  $L_s = 275^\circ$  [4], [5]. The high total dust opacity was mainly found over tropics. [4], [5].

The next mission which monitored extensively the Martian atmosphere including the dust load was the Mars Global Surveyor (MGS) using the Thermal Emission Spectrometer (TES) [6], [7] and the Mars Orbiter Camera (MOC) [8], [9] for three Martian years. Images taken by MOC during  $L_s = 107^\circ$  and  $L_s = 274^\circ$  of MY 24 showed around 783 dust storms, ranging in size from “local” ( $>100 \text{ km}^2$ ) to “regional” ( $>1.6 \times 10^6 \text{ km}^2$ ) [8]. The spatial maps produced from TES measurements illustrated two events of ‘regional dust storm’ in MY 24 (1999) starting in different locations over tropics and time [6]. A planet-encircling dust storm was observed by both instruments in MY 25 (2001) at  $L_s = 194^\circ$  starting from a local dust storm that appeared at  $L_s = 185^\circ$  near Hellas [10], [11], [9]. The onset, expansion and end of the global dust storm were presented by spatial maps showing mostly high dust abundance over the southern hemisphere up to  $30^\circ\text{N}$  [10].

The global dust storm in MY 28 (2007) occurred just before the southern summer solstice. It was observed by two instruments in the infrared spectral range, namely, the THEMIS (Thermal Emission Imaging System) aboard the Mars Odyssey spacecraft [12] and the PFS instrument on board Mars Express (MEx, [13]). The seasonal dust variability was described by [14] using the dataset composed of measurements obtained from TES, THEMIS and MCS (Mars Climate Sounder, [15]) aboard the MRO (Mars Reconnaissance Orbiter) spacecraft during eight Martian years from MY 24 to MY 31.

Dust can be lifted into the atmosphere by sever-

al mechanisms, including surface wind, dust devils and saltation, which can form local, regional and global dust storms [8]. These mechanisms depend on the size of the dust particles. After dust injection into the atmosphere, these can remain from one day until almost 150 days for local and global dust storm, respectively. Dust can be transported by general circulation (baroclinic or planetary waves and the Hadley cell), mesoscale and local winds. However, the mechanism of the origin for the global dust storms is still unknown [10].

In our work, we provide global characterization of the dust activity observed by the PFS during six full Martian years [16]. Our analysis presents different dust behaviors varying with season and latitude. Therefore, we distinguish the typical Martian year and the encircling planet dust storm that occurred in MY 28. We show the effect of dust on atmospheric temperatures by calculating heating and cooling rates during heavy, moderate and low loads of atmospheric dust.

## Dust activity in dusty season:

The spatial variations of the dust opacity during the southern spring and summer are presented in **Fig. 1**. We build maps of dust for  $20^\circ$   $L_s$ ,  $3^\circ$  latitude and  $5^\circ$  longitude bins for each Martian year, and we find out similar behavior of the dust opacity variations from  $L_s = 180^\circ$  to  $360^\circ$  over several years, except for MY 28. Therefore, we select maps with most evident features to illustrate the evolution of the dust atmospheric content in the second half of the Martian year. We present the dust evolution from  $L_s = 180^\circ$ , because of the higher dust opacity (0.3) which is not observed earlier in the year. In the period ranging from  $L_s = 180^\circ$  to  $200^\circ$ , the dust activity develops over the South-West regions of Hellas, where slope winds and dynamical processes can efficiently lift up the surface dust to the atmosphere. Regional dust storms are also observed northward of Hellas, at Syrtis, close to Isidis Planitia, and over Chryse Planitia. Some significant dust amounts are observed closer to the South Pole. Wang and Richardson (2015) [17] also noted some expansion of the dust toward the North and East regions from Hellas, based on MOC and MARCI images, which is in agreement with our results. They found out that the possible routes for the southern sequences (dust occurrences) are at locations where the GCM model

predicts high surface wind stresses. As the dust lifting continues, it begins to be transported northward by the global circulation. Dust opacities larger than 0.4 are also observed in the southernmost regions during local spring and summer seasons, resulting from the sublimation of the South polar cap, where the dust trapped in the ices is released into the atmosphere. Unexpected medium dust load values are also retrieved over latitudes higher than 60°N during the cold seasons. These are likely CO<sub>2</sub> ice particles retrieved as dust.

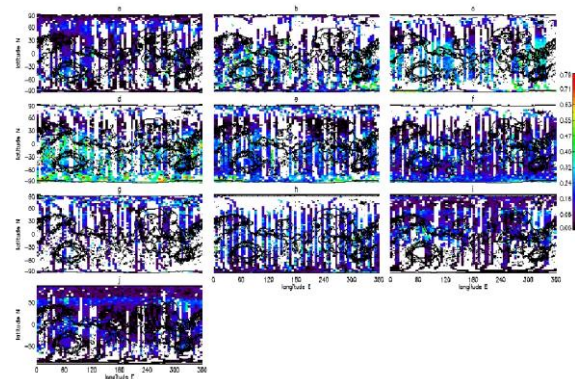


Fig.1. Spatial maps of total dust opacities with a topography contour for a typical Martian year during: a. Ls = 180° - 200°, b. Ls = 200° - 220°, c. Ls = 220° - 240°, d. Ls = 240° - 260°, e. Ls = 260° - 280°, f. Ls = 280° - 300°, g. Ls = 300° - 320°, h. Ls = 320° - 340°, i. Ls = 340° - 360°, j. Ls = 0° - 20°.

The maximum extent of the dust opacity is reached from Ls = 240° to 260°, when it is observed over the whole Southern hemisphere, and up to 30°N. On the contrary, low values of dust opacity (< 0.1) are found over northern mid-latitude regions, during the Ls = 210° to 300°. The observed spatial dust dichotomy (Fig. 1) appears associated with the N-S topographic dichotomy line on Mars [18].

From Ls = 300°, the dust starts developing over the mid-latitude northern regions, with larger values at the end of year and at the beginning of the following year. The dust opacity increase observed around 60°N for all longitudes starting from Ls = 340° originates from the sublimation of the North polar cap edges during the spring season. Peculiar regions of persistently high dust opacity are also evident in the Northern hemisphere during the main dust activity season. More specifically, regional dust storms are likely occurring over Tyrrena Terra and Chryse Planitia at Ls = 200 - 280°, and over Acidalia Planitia and Tyrrena Terra at the end of the year (Ls = 340° - 360°).

#### Global dust storm in MY28:

The onset of a global dust storm could be characterized by the coalescing of multiple regional storms [9]. During the planet-encircling dust storm observed in 2007 (MY 28), the seasonal and spatial evolution of dust activity showed peculiar behavior.

In this work we consider the beginning of the global dust storm of MY 28 to be when the dust opacity over some places gets larger than 0.4. This happens from Ls = 200° (Fig. 2).

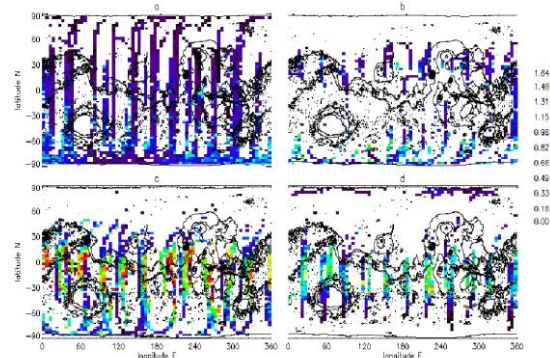


Fig.2. Spatial maps of total dust opacities with a topography contour for the global dust storm in MY 28 during: a. Ls = 200° - 235°, b. Ls = 235° - 270°, c. Ls = 270° - 305°, d. Ls = 305° - 340°.

Significant amounts of dust are lifted up in the atmosphere over the south polar regions, close to the west side of Hellas and Noachis areas, while some preceding occurrences of atmospheric dust are also observed over Chryse Planitia at Ls = 180°; this is also seen by MOC and on MARCI images [17] but later in the season, namely, at Ls = 260°. Unfortunately, we are not able to deeper investigate the seasonal variations between Ls = 230° and 270°, because of PFS sparse data. However, Wang and Richardson (2015) [17] suggested that the dust from the region Chryse Planitia was moved to Noachis Terra by means of cloud transport. The dust cloud travel from North to South is still ambiguous, because of the lack of images from MARCI. Also, some calculations showed that this transport requires a continuous wind speed of around 25 m/s during the full day, condition which is not possible to meet [19].

In contrast to a typical Martian year, the maximum of dust activity in MY 28 (see Fig. 2) is found later at Ls = 270°, and high amounts of dust persist in the atmosphere until Ls = 305° over most of the tropical and sub-tropical regions (30°S - 30°N of latitude). In this period, the total dust opacity exceeds 2 for some locations. In the Ls interval of 305° to 340°, the high dust opacity is still present, while, during a typical Martian year, the total dust opacity is already low, i.e. less than 0.2. The heavy loads of dust during the maximum activity are mostly observed over low northern and southern latitudes. The PFS observations of global dust storm in MY 28 are consistent with THEMIS observations [12].

#### Heating and cooling rates during high, moderate and low amount of dust in the atmosphere:

Heating and cooling effects of dust are estimated in the infrared range from 7.87 - 10.31 μm (1270 -

970  $\text{cm}^{-1}$ ) and in the visible range at 0.67  $\mu\text{m}$  (0.66 – 0.68  $\mu\text{m}$ ). Our purpose is to show vertical profiles of heating and cooling rates during high, moderate and low dusty condition for selected measurements, and to investigate the effects of dust on atmospheric temperatures. Four PFS measurements from orbits 4510, 4471, 4328 and 4428 have been selected in the latitude belt between 25°S and 45°S during the global dust storm of MY 28. The corresponding PFS-retrieved dust column-integrated optical depths are 1.73, 1.46, 0.41, 0.16, respectively. All measurements were acquired in the afternoon, between 12 and 15 h LT, to assure the highest impact of solar insolation.

In order to compute the heating and cooling rates we used the temperature profiles retrieved from PFS, and the vertical distribution of dust opacity derived from measurements by the MCS – MRO. In this study we used the formula for the dust vertical distribution derived from the MCS dataset of dust opacities (Eq.15 in [20]). We first selected MCS dust profiles in MY 29, from  $L_s = 240^\circ$  to  $275^\circ$  and for latitude region between 25°S and 45°S selected, and with a goodness of fit  $R^2 > 0.98$ . Then, we made our calculations by using either a “typical” (most common) dust profile in this selection, and dust vertical profiles selected to be as close as possible in time and in place to the selected PFS observations (**Fig. 3**). We also used MCS dust profiles in MY 28 averaged for a region from 30°S to 30°N at  $L_s = 280^\circ$  provided by N. Heavens (private communications). The net heating and cooling rates calculated for the vertical dust distributions from MY 28 and MY 29 are plotted in **Fig. 4a, b and c**. They show in principle a similar effect of dust on thermal balance in the atmosphere. We observe a significant net heating of atmospheric layers above the maximum peak of dust profile induced by solar radiation. The net heating rate increases with total dust opacities. **Fig. 4c** presents maximum of net heating and cooling rates higher in altitude and in values than in **Fig. 4a, b** due to the higher altitude of peak for the dust vertical distribution in MY28 (**Fig. 3**).

In all cases, the atmospheric layers above the altitude of max dust opacity are strongly heated. The maximum heating is always observed at altitudes about 15-20 km higher than the altitude of max dust opacity in the MCS profiles. Net heating rates as high as 40-50 K/day are derived for moderate dust loads in MCS profiles during regional dust storms in MY 29, and as high as 60-80 K/day during the global dust storm of MY 28. Even low amount of dust around 0.16 produces the net heating rate of a few kelvins per day which is consistent with work done by [21]. Previous calculations of heating rates presented by [22] and [23] showed similar results of 80 K/day and 70 K/day, respectively, for heavy loads of dust in the atmosphere which are in good agreement with our calculations. However, it is necessary to highlight

that the numbers strongly depend on both optical properties and vertical distributions of dust [23].

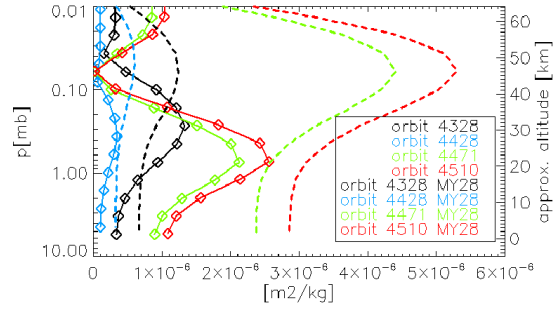


Fig. 3. MCS dust vertical distributions in MY 29 and MY 28 (dashed lines) normalized to PFS total dust opacities around 1.73 (orbit 4510), 1.46 (orbit 4471), 0.41 (orbit 4328), 0.16 (orbit 4428).

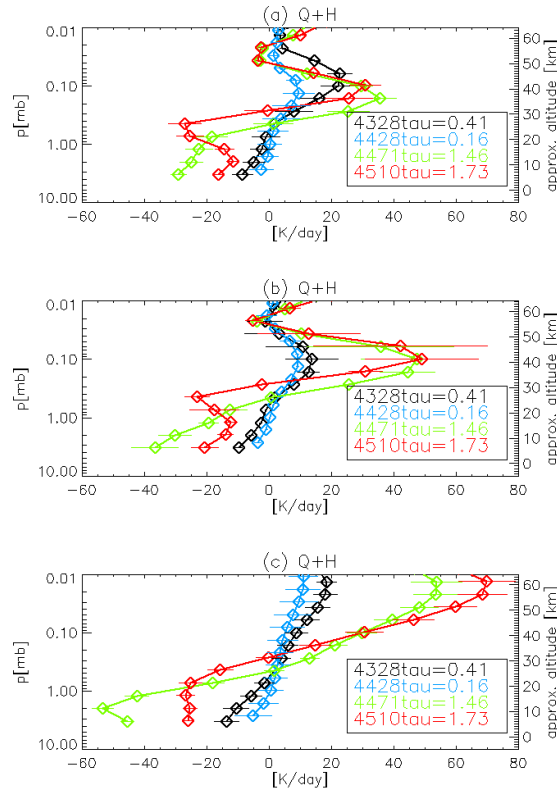


Fig. 4. Net heating and cooling rates for different dust vertical distribution: (a) same location and LT of PFS temperature profiles (MY 29b) ; (b) typical (MY 29); (c) averaged during MY 28 dust storm.

Contrary to the heating, the cooling of atmosphere due to the dust is evident close to the surface and in the lower layers of the atmosphere. However, the intensity of net cooling rate depends on the total dust opacity (**Fig. 4a, b and c**). For dusty atmospheres, the cooling is not particularly effective near the surface due to green-house effect by dust. Indeed, photons are trapped in the lower part of the atmosphere and cannot escape to the space, being blocked and

re-emitted by the optically thick dust layers at higher altitudes. The highest dust opacity (1.73) generates a net cooling of ~30 K/day in the altitudes of maximum dust opacity. The cooling rates decrease for lower altitudes. An opposite behavior is observed for moderate to low opacities, where the cooling is maximum near the surface and decreases with altitude. No significant differences are found in the net heating and cooling rates for low dust opacity.

#### **Uncertainty of heating and cooling rates:**

The shape of vertical profile as well as the total content of dust are key parameters in the calculation of vertical profile for heating and cooling rates in the atmosphere. Unfortunately, there are no MCS retrievals of dust profiles simultaneous to PFS observations. As a consequence, we can only make assumptions of vertical dust distributions. In **Figure 4a and 4b** we compare the calculated heating and cooling rates by using typical (Fig. 4b) and closest (Fig. 4a) dust profiles in MY29. The results are very similar, the differences being of the order of 5-10 K/day everywhere except around the altitudes of maximum heating, where the differences are as large as 20-30 K/day (see errorbars in Fig. 4b). We also investigated the influence of uncertainties of the PFS temperature profile and total dust opacities on calculations of heating and cooling rates under an assumption that the dust vertical distribution derived from the MCS dataset represents the real atmospheric condition without error. The final errors of net heating and cooling rates (**Figs 4a and 4c**) are within the uncertainties due to different dust vertical distributions (**Fig. 4b**).

#### **Conclusions:**

The dataset of PFS-retrieved atmospheric parameters [16] allowed us to characterize the dust activity on Mars for six full years. We demonstrate the temporal and spatial distribution of column-integrated dust optical depths derived from PFS observations during dusty season in MY 28 and in other Martian years. The dust evolution differs during the global dust storm in 2007 (MY 28) from the 'typical' Martian year considered in this study. Namely, the high dust activity starts later in MY 28 and lasts longer than in other Martian years. The south-west of Hellas and south polar regions might be considered as an onset of the global dust storm in 2007 (MY 28). The region along 60°S probably associated with the edge of receding polar cap shows dust increases at the beginning of dusty season in the 'typical' Martian year. At maximum activity, dust is mostly evident over the southern hemisphere up to 30°N in the 'typical' Martian year and concentrated in tropics in MY 28.

We also study the dust effect on atmospheric temperatures in terms of heating and cooling rates. The net heating and cooling rates showed heating of

the atmosphere above and in the upper part of the dust layer and cooling below up to the surface. The vertical profile of net heating and cooling rates strongly depends on the dust vertical distribution and its content in the atmosphere.

#### **Acknowledgements:**

This work is conducted as part of the project UPWARDS-633127, funded by the European Union's Horizon 2020 Programme (H2020-Compet-08-2014).

#### **Bibliography:**

- [1] Hanel, R.A. et al., *Science*, 175, 305-308, 1972;
- [2] Fenton et al., *Icarus*, 130, 115–124, 1997; [3] G. Lee, *Science*, 194, 59 – 62, 1976; [4] Martin T. Z., *Icarus*, 66, 2—21, 1986; [5] Martin T. Z. and M. I. Richardson, *J. Geophys. Res.*, Vol. 98, No. E6, 10,941-10,949, 1993; [6] Smith M.D. et al., *J. Geophys. Res.*, vol. 106, NO. E10, 23929 – 23945, 2001; [7] Smith M. D., *Icarus*, 167, 148-165, 2004; [8] Cantor B. A. et al., *J. Geophys. Res.*, vol. 106, No. E10, 23,653 – 23,687, 2001; [9] Cantor B. A., *Icarus*, 186, 60 – 96, 2007; [10] Smith M. D. et al., *Icarus*, 157, 259 – 263, 2002; [11] Strausberg et al., *J. Geophys. Res.*, vol. 110, E02006, 2005; [12] Smith M. D., *Icarus*, 202, 444 – 452, 2009; [13] Chicarro, A. F. et al., ESA-SP 1240, pp. 3 – 16, 2004; [14] Montabone L. et al., *Icarus*, 251, 65 – 95, 2015; [15] McCleese et al., *J. Geophys. Res.*, vol. 112, E05S06, 2007; [16] Giuranna et al., [this workshop](#); [17] Wang H. and M. I. Richardson, *Icarus*, 251, 112 – 127, 2015; [18] Smith, D.E. et al., *Science*, 284, 1495-1503, 1999; [19] Wilson R. J. and K. Hamilton, *J. Atm. Sci.*, vol. 53, No.9, 1290, 1996; [20] Heavens N.G. et al., *J. Geophys. Res.*, vol. 116, E04003, 2011; [21] Moriyama S., *Journal of the Meteorological Society of Japan*, Vol. 53, No. 3, 1975; [22] Zurek R. W., *Icarus*, 35, 196 – 208, 1978; [23] Savijarvi H. et al., *Q. J. R. Meteorol. Soc.*, 131, pp. 2907–2922, 2005